*Article*

# Introduction of a Novel Technique in Density-Adjusted 3D Printing for the Manufacture of Soft-Tissue-Equivalent Radiological Phantoms

**Ismail Ozsoykal and Ayşegül Yurt ***

Medical Physics Department, Health Sciences Institute, Dokuz Eylul University, Izmir 35320, Turkey;
ismail.ozsoykal@ogr.deu.edu.tr
* Correspondence: aysegul.yurt@deu.edu.tr

**Abstract:** The aim of this study is to introduce a new filament and novel 3D printing technique to adjust the density of a printing job in order to mimic the radiological properties of different tissues. We used a special filament, Light Weight PLA (LW-PLA), which utilizes foaming technology triggered by temperature. Cylindrical samples were printed at various temperatures, flow rates, print speeds, and diameters. A computed tomography (CT) scan was performed to identify their radiological properties in terms of the mean Hounsfield Unit (HU). The densities of the samples ranged from 0.36 $g/cm^3$ to 1.21 $g/cm^3$, corresponding to mean HU values between $-702.7 \pm 13.9$ HU and $+141.4 \pm 7.1$ HU. Strong linear correlations were observed between the flow rate and density as well as the flow rate and mean HU. The axial homogeneity of the samples was reported as being comparable to that of distilled water. A reduction in the mean HU was observed at a lower print speed and it changed slightly with respect to the sample size. Reproducibility assessments confirmed consistent results for identical printing jobs. Comparisons with regular PLA samples revealed a superior homogeneity in the LW-PLA samples. The findings of this study suggest a practical and accessible solution for mimicking all of the soft tissues, including the lungs, by using a single filament.

**Keywords:** 3D printing; density modulation; soft tissue; computed tomography; phantom

## 1. Introduction

Recent advancements in 3D printing technology have enhanced its utility and led to the cost-effective in-house production of customized tools across various fields. In the field of medical physics, there is an increasing number of studies focusing on the printing of imaging and dosimetry phantoms to be used in radiology, radiation oncology, and nuclear medicine departments [1–4]. It is important for an imaging or dosimetry phantom to mimic the radiological properties of the tissue or tissues that are the subject of interest to perform a particular clinical task. In the context of 3D printing, this goal can be achieved by adjusting the density of the printed part to match the density of the target tissue. This could be achieved by either selecting a printing material with an appropriate density or choosing appropriate printing parameters to adjust the density of the printed object.

Fused Deposition Modeling (FDM) is one of the 3D printing technologies that has gained widespread use due to offering users a broad spectrum of printing materials with a wide range of physical properties, which continues to grow over time. This makes FDM technology a major breakthrough for producing a variety of tissue-mimicking radiological phantoms. The radiological properties of commercially available FDM 3D printing filaments have been investigated in many studies by performing computed tomography (CT) scans and reporting the Hounsfield Unit (HU), since it provides a quantitative measure of the X-ray attenuation coefficient, thus allowing for the analysis of tissue equivalency [5–10]. For a typical body habitus, HU values range from around $-900$ HU to well above $+1000$ HU, corresponding to tissues such as the lungs and compact bone, respectively [11].

Notably, Ma et al. conducted an extensive study encompassing a wide array of filaments from different vendors with densities between 0.75 g/cm$^3$ and 1.70 g/cm$^3$. The samples, all printed at a maximum achievable material density, yielded a range of HU values, spanning approximately from $-250$ to $+1000$, following a CT scan performed at 120 kVp [12]. This study has proven that it is possible to mimic most of the tissues, except the lungs. On the other hand, even higher HU values have been achieved in different studies experimenting on new commercial filaments and their printing methods [13–15]. Even further, there are studies that focused on the manufacture of bismuth and barium sulfate-infused Acrylonitrile Butadiene Styrene (ABS) filaments to fabricate very dense materials for radiation protection [16,17].

On the contrary, despite the abundance of high-density filaments, no filament option exists with a physical density as low as that of the lungs. This has prompted numerous studies focusing on regulating specific printing parameters in FDM printing to reduce the amount of filament deposited per unit volume, thereby decreasing the density of the printed object. Initial efforts have been concentrated on decreasing the infill rate; in other words, increasing the spacing between the printed lines on the axial plane. Unfortunately, this method has yielded unfavorable results, manifesting as increased uncertainties and inhomogeneities at lower infill rates [14,15,18–22]. Several studies that adopted this approach resulted in lung phantoms with unrealistic tissue textures [18,21–24]. On the other hand, some recent studies aimed to adjust the density of a printing job via the modulation of the flow rate and print speed [25,26]. Both parameters were used to govern the printed line width, rather than spacing between the printed lines. This allowed for the subpixel printing of lines and presented much better results in terms of homogeneity and texture control. Both novel approaches in both studies have been integrated into computational algorithms designed to read DICOM images on a voxel basis and generate a 'G-code' that contains adjustments to the flow rate or print speed, calibrated to achieve reference voxel-based densities, i.e., HU values. However, these algorithms are not accessible, and creating similar algorithms could be a challenging task for the majority of researchers. Therefore, the need for practical and accessible methods to mimic low-density tissues such as the lungs still stands.

The recent introduction of special filaments has paved a new way for printing low-density parts. One of these filaments is Light Weight PLA (LW-PLA), which was introduced by colorFabb. Differing from other PLA-based regular filaments, LW-PLA has the unique feature of utilizing active foaming technology triggered by the temperature. The expansion resulting from foaming allows users to achieve similar line widths with reduced flow rates at higher temperatures. Overall, this makes it possible to decrease the density of a 3D-printed object without compromising either the infill rate or the line width, thus maintaining a much higher level of homogeneity.

Taking into account the developments of 3D printer technologies and new filament materials, this study aims to investigate the impact of the printing temperature, flow rate, print speed, and print size on the physical density and corresponding HU values of 3D-printed LW-PLA samples.

## 2. Materials and Method

This study was conducted in three parts. The first part involved the analysis of the radiological properties of the LW-PLA samples printed at different temperatures and flow rates. This part also included 3D-printed samples with a regular PLA filament as a blank control, aiming to highlight the differences arising from the foaming feature of LW-PLA. The second part was dedicated to testing the reproducibility of the printing process. The third part was designed to investigate the effects of both the print size and print speed on the print job. The detailed structure of this study is described in the following section.

*2.1. 3D Printing Cylindrical LW-PLA Samples for Radiological Characterization*

In this study, a Raise3D Pro2 Plus printer (Raise3D, Irvine, CA, USA) was utilized with a 0.4 mm diameter nozzle. Prior to the printing process, ideaMaker 4.3.2 (Raise3D, Irvine, CA, USA) was used as the slicing software to generate the G-code for the cylindrical models. All models had identical dimensions of 1.5 cm diameter and 2 cm height (Figure 1). Samples were printed with a 1.75 mm diameter LW-PLA filament from Colorfabb in Belfeld, Netherlands. This filament is special for its foaming at around 220 °C and above, which allows for a reduced density at the nozzle exit. The ability to control the density of the filament material specifically at the nozzle exit is crucial for having prints at lower densities, without making any changes (i.e., reduction) to the infill rate.
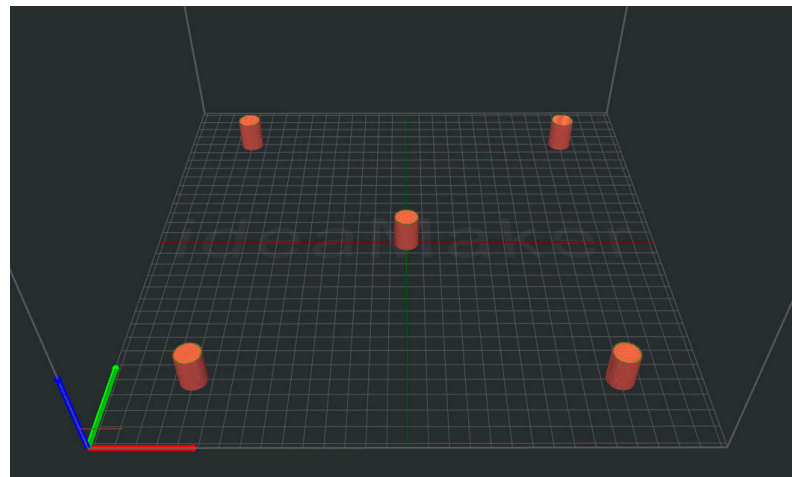


**Figure 1.** Preview of the printing setup in ideaMaker for a group of cylindrical samples. Each setup features a fixed printing temperature but varying flow rates among the samples.

Cylindrical samples were printed in six groups of printing temperatures, ranging from 200 °C to 250 °C in increments of 10 °C. Each group was printed with 5 specific flow rate settings, as detailed in Table 1. Other main printing parameters, such as the infill rate, print speed, layer thickness, and fan speed, were held constant across all printing jobs, set at 100%, 33 mm/s, 0.15 mm, and 50%, respectively. The infill pattern was chosen as 'lines'.

**Table 1.** Printing temperature and flow rate settings for 30 cylindrical LW-PLA samples.

| Temperature (°C) | Flow Rate (%) | | | | |
|---|---|---|---|---|---|
| 200 | 100 | 90 | 80 | 70 | 60 |
| 210 | 100 | 90 | 80 | 70 | 60 |
| 220 | 90 | 80 | 70 | 60 | 50 |
| 230 | 80 | 70 | 60 | 50 | 40 |
| 240 | 70 | 60 | 50 | 40 | 30 |
| 250 | 60 | 50 | 40 | 30 | 20 |

For temperatures of 220 °C and above, the maximum applied flow rate was deliberately decreased in increments of 10%. This adjustment aimed to prevent any printing artifacts, such as swelling of the print due to overexpansion induced at high printing temperatures. This phenomenon is clearly demonstrated in Figure 2, which depicts two samples: one printed with LW-PLA and the other with regular PLA (Porima, Turkey). Both samples were printed at a temperature of 250 °C and a flow rate of 100%. As is evident, the LW-PLA sample exhibited overexpansion, resulting in printing artifacts, whereas this is not observed in the sample printed with regular PLA.
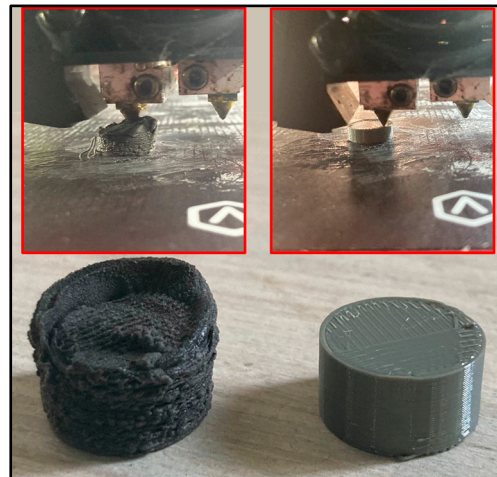
**Figure 2.** Cylindrical samples were both printed at 250 °C and 100% flow rate. The LW-PLA sample (left) exhibited overexpansion due to excess flow, resulting in an unintended geometry of the print job.

In addition to the cylindrical LW-PLA samples, a set of cylindrical regular PLA samples were printed with identical dimensions to serve as blank controls. The printing temperature was chosen as 230 °C, which was the maximum value recommended by the vendor. Flow rates were set as 100%, 80%, 60%, 40%, and 20%. All other printing parameters were kept constant.

### 2.2. Testing for the Reproducibility of the Print Job

Following the printing of the primary LW-PLA samples, the printing process was repeated twice for all flow rates applied to three temperature groups: 210 °C, 230 °C, and 250 °C. This resulted in 30 additional samples, allowing for the analysis of reproducibility.

### 2.3. Investigating the Effect of Print Size and Print Speed

The LW-PLA filament is sensitive to heat transfer, which can be defined as a function of the printing temperature, flow rate, print speed, and cooling fan speed. In addition to these parameters, the horizontal cross-section may also play a role in the heat energy transferred to consecutive layers. Printing objects with a small cross-sectional area on the x–y plane means that the nozzle will travel more frequently across consecutive layers, potentially leading to higher heat exposure for each layer compared to print jobs with larger cross-sectional areas.

For this reason, this part of the study aimed to investigate the effect of the print size on the horizontal plane by printing three cylindrical samples with diameters of 1.5 cm, 3.5 cm, and 5.5 cm. The height of the samples was held constant at 2 cm. These samples were printed at 250 °C and a 60% flow rate with a print speed of 27 mm/s. This approach enabled us to interpret the influence of the print speed by comparing the findings from the 1.5 cm diameter samples printed at different speeds (33 mm/s and 27 mm/s), both in this part and earlier in the first section of this study.

### 2.4. Data Collection and Analysis

Prior to CT imaging, the mass of each sample was measured using an analytical balance, Weightlab WSA-224 (Weightlab Instruments, Istanbul, Turkey), with a sensitivity of 100 μg (Figure 3). Accordingly, the physical densities of the samples were calculated and recorded.
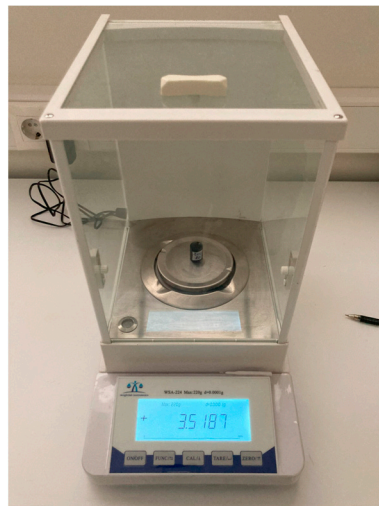
**Figure 3.** All of the samples weighed using Weightlab WSA-224 analytical balance.

After determining their densities, the printed samples were affixed to PMMA disks, which were designed and fabricated before, as in Figure 4a. Subsequently, these disks were positioned within a cylindrical PMMA housing, characterized by its 0.5 mm thick walls, 15 cm inner diameter, and 30 cm length (Figure 4b). The bottom plate of the housing was securely affixed with silicone, while the top plate was designed to be remountable, utilizing a liquid seal and four screws. To ensure stability during horizontal scanning, a pair of support materials was thoughtfully designed. Distilled water was introduced into the housing to establish the 'water phantom', as illustrated in Figure 4c.
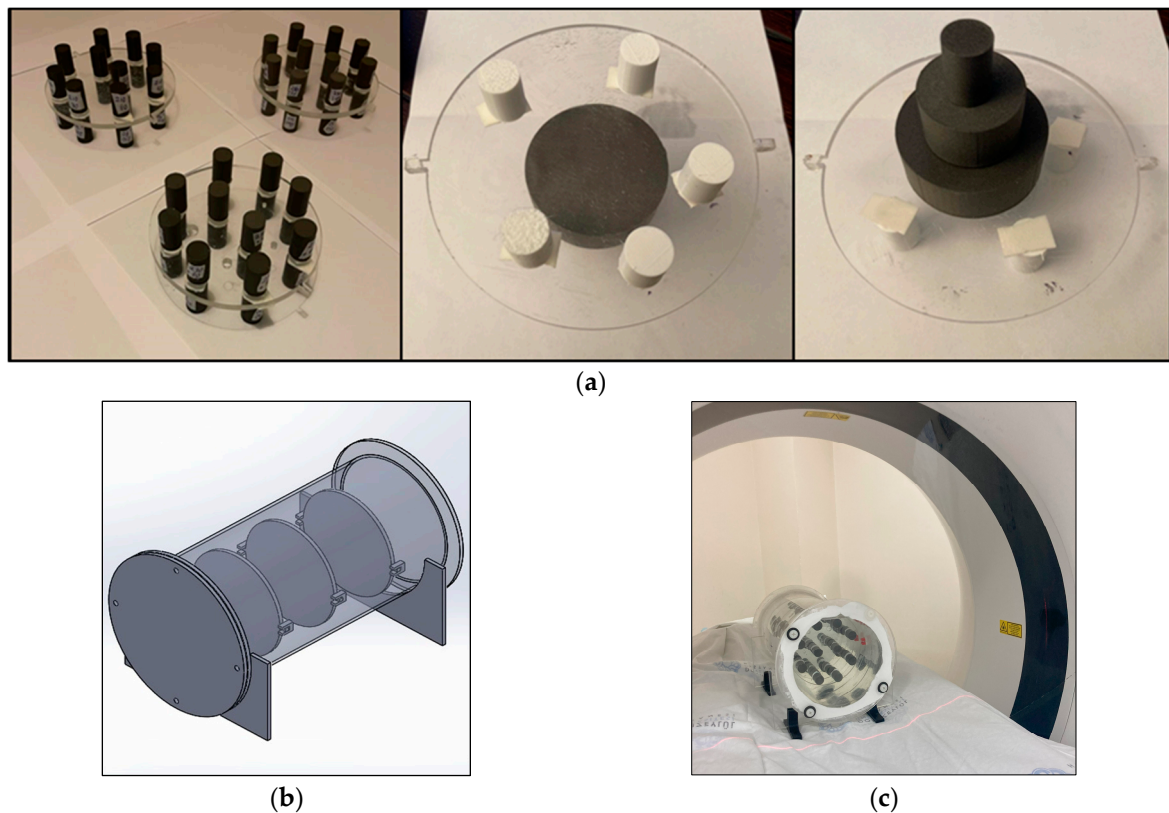


(a)



(b)



(c)

**Figure 4.** Printed samples mounted on PMMA disks (**a**), which were placed in a water phantom (**b**) prior to a CT scan (**c**).

The water phantom has been imaged using a 128-slice Philips Ingenuity CT scanner. Imaging protocol includes a tube voltage of 120 kVp and effective tube current–time product of 310 mAs. The reconstructed slice thickness was 0.4 mm with a collimation of $64 \times 0.625$ mm per rotation. $CTDI_{vol}$ was recorded as 20.3 mGy in the body phantom, while SSDE was 46.1 mGy. The image reconstruction diameter, namely field of view (FOV), was 250 mm with a $512 \times 512$ matrix, resulting in a pixel size of $0.488 \times 0.488$ mm$^2$.

Following the CT scan, the CT image was loaded into imQuest, a practical CT image analysis tool developed by Duke University and made available online [27]. Data collection involved drawing circular regions of interest (ROIs) with a diameter of 1 cm on 30 consecutive axial slices in the central portion of each sample. Mean HU values and their standard deviations (STDs) were recorded for every slice, as illustrated in Figure 5, and then averaged over the 30 slices. Additionally, the standard deviation of the mean HU values was calculated as a measure of the homogeneity along the longitudinal axis. For simplicity, the average of the axial STD values is referred to as $STD_{xy}$ notation, while $STD_z$ is used for the STD of the mean HU values across the 30 slices.
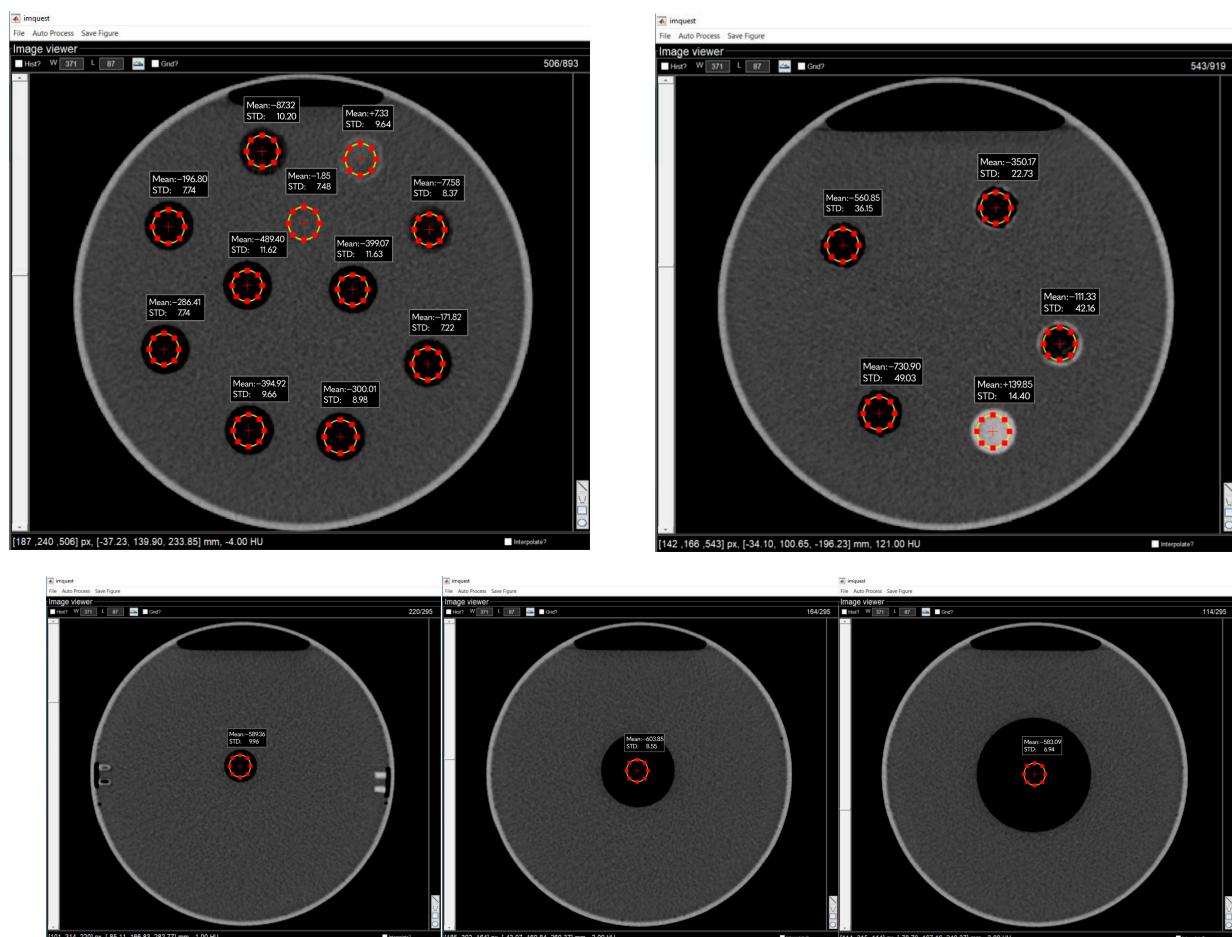


**Figure 5.** The mean Hounsfield Unit (HU) and standard deviation (STD) were measured by drawing circular regions of interest (ROIs) with a diameter of 1 cm at the center of each cylindrical sample, as well as within water, across 30 consecutive slices.

The reproducibility of the samples was analyzed by averaging the mean Hounsfield Unit (HU) values obtained from three consecutive identical printing jobs and calculating the standard deviation across them. On the other hand, one-way ANOVA tests were performed to analyze the differences among the mean HU and $STD_{xy}$ values obtained from the sample groups with diameters of 1.5 cm, 3.5 cm, and 5.5 cm. Subsequent tests, such as Tukey

and Tamhane, were conducted to identify the specific group or groups responsible for the observed differences.

## 3. Results

### 3.1. LW-PLA Samples

The results of the 1.5 cm diameter LW-PLA print jobs are illustrated in Table 2. The density of the samples printed at different temperatures and flow rates were found between 0.36 g/cm$^3$ and 1.21 g/cm$^3$ that correspond to mean HU values between $-702.7$ HU and $+137.6$ HU, respectively. Simple linear regression models were used to examine the relationships between the flow rate and density, flow rate and mean HU, and density and mean HU. These models demonstrated a strong fit to the data, as illustrated in Figure 6 ($R^2 > 0.99$).
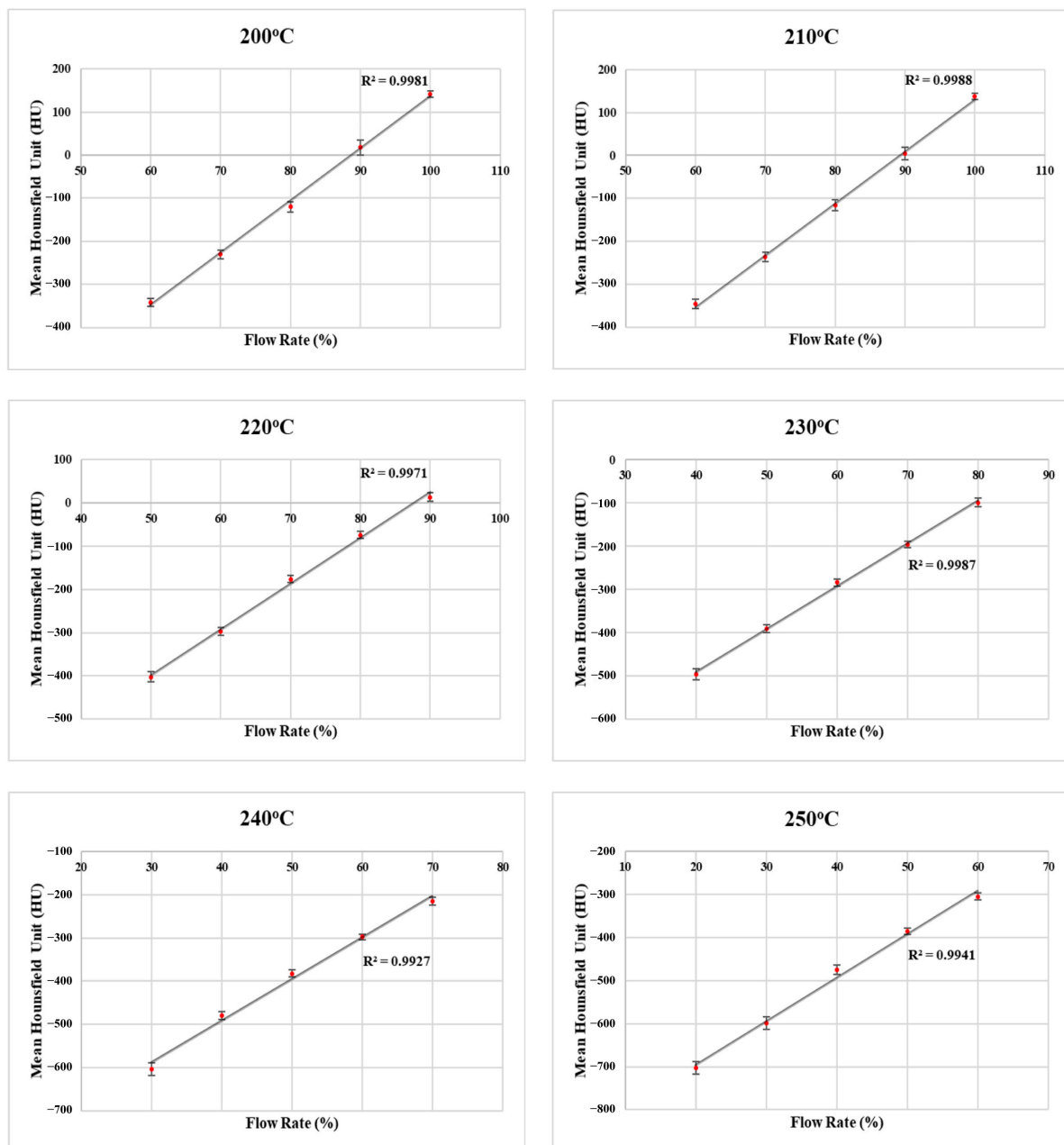


**Figure 6.** Simple linear regression models of flow rate versus mean HU obtained at printing temperatures ranging from 200 °C to 250 °C for LW-PLA samples. $STD_{xy}$ values are illustrated in bars.

**Table 2.** LW-PLA findings of mass, density, mean Hounsfield Unit (HU), standard deviation on axial plane ($STD_{xy}$), and along longitudinal axis ($STD_z$) under different printing temperatures and flow rates.

| Printing Temperature (°C) | Flow Rate (%) | Mass (g) | Density (g/cm³) | Mean HU | ±$STD_{xy}$ | ±$STD_z$ |
|---|---|---|---|---|---|---|
| 200 | 100 | 4.22 | 1.19 | +141.4 | 7.1 | 1.1 |
|  | 90 | 3.88 | 1.10 | +17.6 | 16.7 | 9.0 |
|  | 80 | 3.52 | 1.00 | −119.6 | 11.9 | 5.1 |
|  | 70 | 3.15 | 0.89 | −230.2 | 9.6 | 2.3 |
|  | 60 | 2.79 | 0.79 | −340.7 | 9.1 | 3.4 |
| 210 | 100 | 4.27 | 1.21 | +137.6 | 7.3 | 2.1 |
|  | 90 | 3.86 | 1.09 | +4.0 | 14.6 | 2.2 |
|  | 80 | 3.49 | 0.99 | −116.3 | 12.5 | 8.9 |
|  | 70 | 3.12 | 0.88 | −237.1 | 10.9 | 4.4 |
|  | 60 | 2.77 | 0.78 | −346.1 | 10.8 | 6.9 |
| 220 | 90 | 3.85 | 1.09 | +13.5 | 10.1 | 5.1 |
|  | 80 | 3.52 | 1.00 | −74.2 | 8.1 | 3.6 |
|  | 70 | 3.13 | 0.89 | −176.1 | 7.6 | 7.4 |
|  | 60 | 2.75 | 0.78 | −296.4 | 9.1 | 4.9 |
|  | 50 | 2.38 | 0.67 | −402.6 | 11.8 | 4.9 |
| 230 | 80 | 3.51 | 0.99 | −98.7 | 9.2 | 7.5 |
|  | 70 | 3.13 | 0.88 | −195.3 | 7.3 | 6.1 |
|  | 60 | 2.77 | 0.78 | −284.2 | 7.6 | 3.6 |
|  | 50 | 2.39 | 0.68 | −390.9 | 9.1 | 4.0 |
|  | 40 | 2.00 | 0.57 | −497.1 | 12.3 | 5.5 |
| 240 | 70 | 3.15 | 0.89 | −215.2 | 9.1 | 1.1 |
|  | 60 | 2.78 | 0.78 | −297.8 | 6.7 | 3.5 |
|  | 50 | 2.42 | 0.68 | −382.5 | 7.9 | 4.3 |
|  | 40 | 2.06 | 0.58 | −479.9 | 9.3 | 3.6 |
|  | 30 | 1.67 | 0.47 | −602.9 | 14.8 | 3.2 |
| 250 | 60 | 2.72 | 0.77 | −304.7 | 7.4 | 6.3 |
|  | 50 | 2.38 | 0.67 | −386.0 | 7.8 | 2.9 |
|  | 40 | 2.02 | 0.57 | −475.8 | 10.9 | 4.7 |
|  | 30 | 1.65 | 0.47 | −599.3 | 14.1 | 1.9 |
|  | 20 | 1.27 | 0.36 | −702.7 | 13.9 | 2.2 |

On the other hand, Figure 7 illustrates various body parts with distinct mean HU values falling within the range achieved by the LW-PLA samples. The highest HU value achievable corresponds to the spongy bone, while the lowest corresponds to the lungs. In between, there are organs such as the heart, liver, stomach, spleen, pancreas, kidneys, and bladder, as well as adipose and muscular tissues, and glandular tissue.

The standard deviation of the mean HU measured in the axial plane ($STD_{xy}$) for the printed samples ranged from ±6.7 to ±16.7, with a median value of ±9.3 HU and a third quartile value of ±11.9 HU. Similar measurements performed on distilled water yielded an $STD_{xy}$ of ±7.5 HU, and mean HU of −1.8 HU. In addition to the assessment in the axial plane, the homogeneity of the samples is also evaluated along the longitudinal axis using

STD$_z$, which ranged from ±1.1 HU to ±9.0 HU. The measurements revealed a median value of ±4.2 HU and a third quartile value of ±5.4 HU. These results are notably higher than the corresponding finding in distilled water, which was measured as ±0.6 HU.
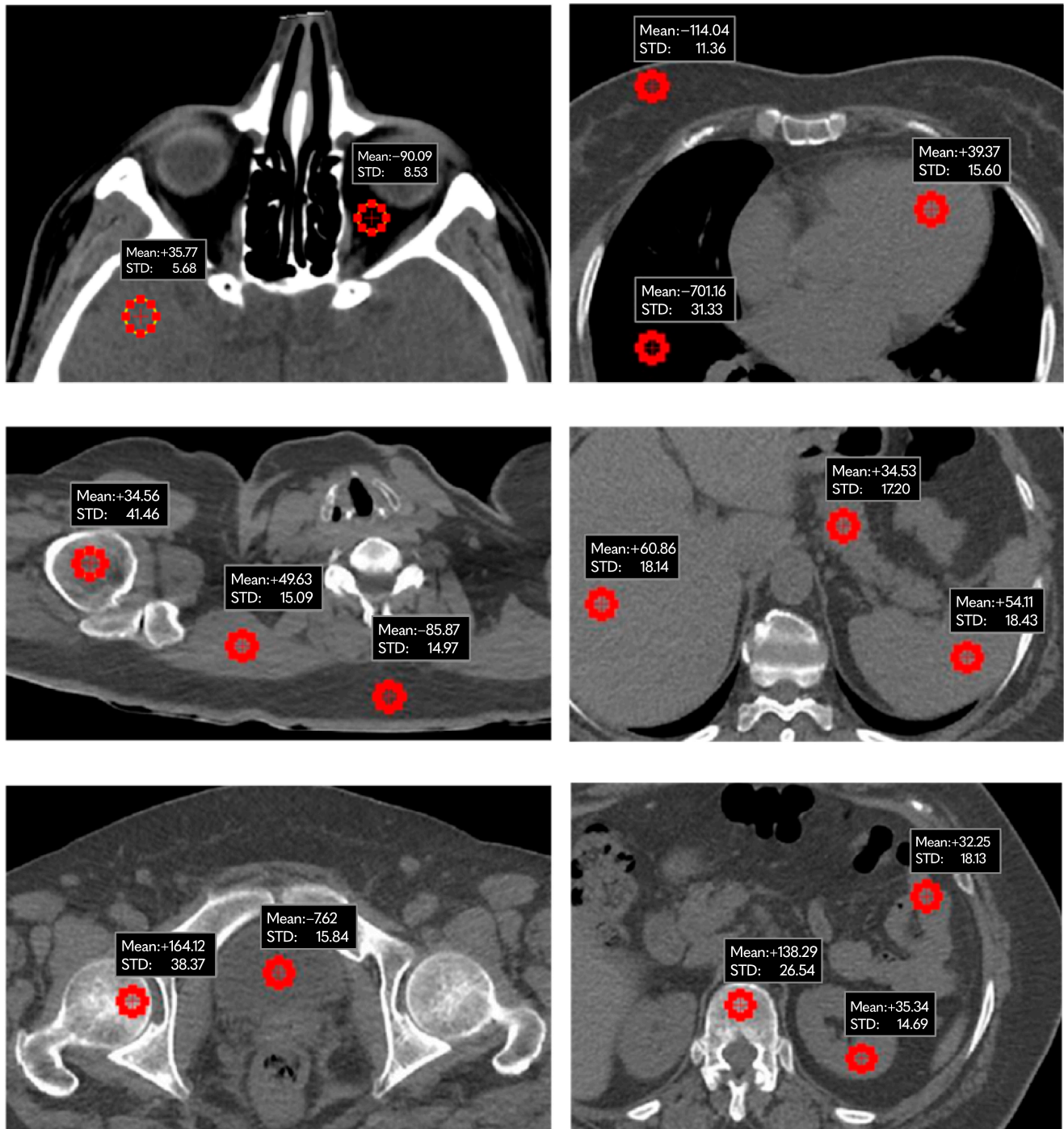


**Figure 7.** Axial CT images from different regions of body encompassing different tissues and organs with different mean HU values that can be replicated by LW-PLA.

## 3.2. Regular PLA Samples

The results of the regular PLA samples that were printed as blank controls are given in Table 3. The density of the printed samples was observed to be very similar to the density of the LW-PLA samples at each flow rate. The mean HU range was obtained between +132.2 HU and −734 HU, which is also similar to the results obtained with the

LW-PLA samples. The $STD_{xy}$ values, however, were observed to be at higher levels for the regular PLA samples. The regular PLA sample printed with an 80% flow rate exhibited an unexpected $STD_{xy}$ value when compared to the findings from the rest of the sample set. This was due to a partial printing artifact observed at the edge of the sample (Figure 8). After drawing an ROI with a smaller diameter for the exclusion of this artifact, it was found that the actual mean HU and $STD_{xy}$ values for this sample are $-85.5$ HU and $\pm 17.2$ HU, respectively.

**Table 3.** Regular PLA findings of mass, density, mean Hounsfield Unit (HU), standard deviation on axial plane ($STD_{xy}$), and longitudinal axis ($STD_z$) under different printing temperatures and flow rates.

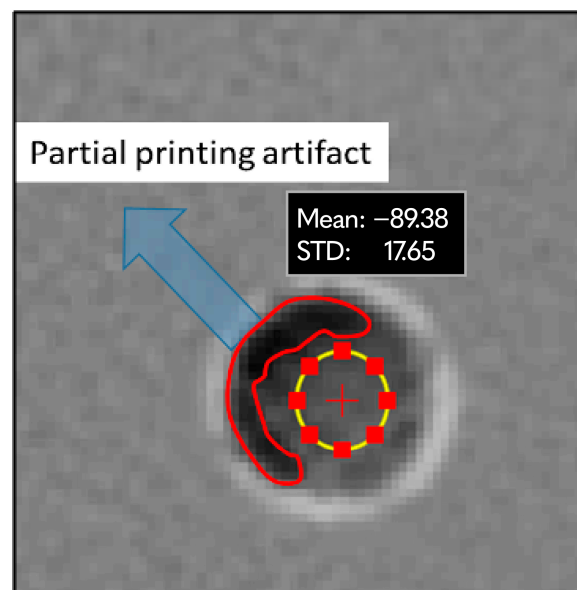| Printing Temperature (°C) | Flow Rate (%) | Mass (g) | Density (g/cm³) | Mean HU | $\pm STD_{xy}$ | $\pm STD_z$ |
|---|---|---|---|---|---|---|
| | 100 | 4.30 | 1.21 | 132.2 | 13.3 | 7.2 |
| | 80 | 3.46 | 0.98 | −106.6 | 41.0 | 10.3 |
| 230 | 60 | 2.80 | 0.79 | −359.8 | 22.4 | 9.1 |
| | 40 | 2.08 | 0.59 | −567.6 | 38.8 | 8.4 |
| | 20 | 1.32 | 0.37 | −734.0 | 47.3 | 3.0 |



**Figure 8.** Partial printing artifact that was detected at the edge of the regular PLA sample printed with 80% flow rate and the correction of measured HU and STD values by drawing a circular ROI with smaller diameter.

Table 4 illustrates the mean HU and $STD_{xy}$ findings of all the regular PLA and LW-PLA samples printed at different temperatures and comparable flow rates. The mean HU values of the regular PLA samples are observed between +132.2 HU and −734.4 HU, which is very similar to the range covered by the LW-PLA samples.

The $STD_{xy}$ values of the regular PLA samples were observed to increase from $\pm 13.3$ HU to $\pm 47.3$ HU as the flow rate was reduced from 100% to 20%, while this trend was not observed in the LW-PLA samples. The $STD_{xy}$ values of the regular PLA samples were observed to be higher than the $STD_{xy}$ values of the LW-PLA samples at all temperatures for each flow rate. This difference was observed to reach a maximum between samples printed with a 20% flow rate (Figure 9). Figure 10, in addition, provides a graphical illustration of the mean HU and STDxy for the regular PLA samples across all flow rates.

Additionally, it includes a subset of LW-PLA samples that have produced mean HU values similar to those of the regular PLA samples.

**Table 4.** Mean HU and $STD_{xy}$ findings of samples printed with regular PLA and LW-PLA at comparable flow rates.

| | Mean HU $\pm$ STD$_{xy}$ | | | | | | |
|---|---|---|---|---|---|---|---|
| Flow Rate (%) | 230 °C Regular PLA | 200 °C LW-PLA | 210 °C LW-PLA | 220 °C LW-PLA | 230 °C LW-PLA | 240 °C LW-PLA | 250 °C LW-PLA |
| 100 | $+132.2 \pm 13.3$ | $+141.4 \pm 7.1$ | $+137.6 \pm 7.3$ | - | - | - | - |
| 80 | $-85.5 \pm 17.2$ * | $-119.6 \pm 11.9$ | $-116.3 \pm 12.5$ | $-74.2 \pm 8.1$ | $-98.7 \pm 9.2$ | - | - |
| 60 | $-359.8 \pm 22.4$ | $-340.7 \pm 9.1$ | $-346.1 \pm 10.8$ | $-296.4 \pm 9.1$ | $-284.2 \pm 7.6$ | $-297.8 \pm 6.7$ | $-304.7 \pm 7.4$ |
| 40 | $-567.6 \pm 38.8$ | - | - | - | $-497.1 \pm 12.3$ | $-479.9 \pm 9.3$ | $-475.8 \pm 10.9$ |
| 20 | $-734.0 \pm 47.3$ | - | - | - | - | - | $-702.7 \pm 13.9$ |

*: Mean HU and $STD_{xy}$ measurements were corrected for partial printing artifact.
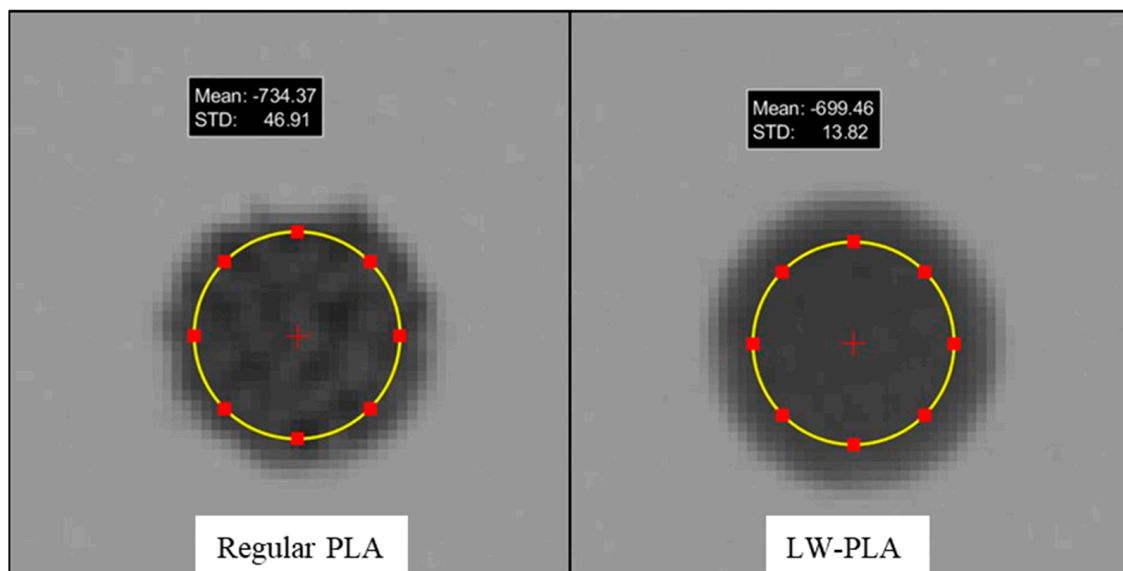


**Figure 9.** Cylindrical samples printed using regular PLA and LW-PLA with a flow rate of 20%.

### 3.3. Reproducibility of the Print Job

The reproducibility of the LW-PLA printing jobs was assessed for three groups of printing temperatures, 210 °C, 230 °C, and 250 °C (Table 5). The STD values among the three jobs ranged from $\pm 1.1$ HU to $\pm 5.9$, with a median value of $\pm 2.7$ HU and third quartile of $\pm 4.5$ HU. Most of the $HU_1$, $HU_2$, and $HU_3$ data fall within one standard deviation of the average. This suggests that the 3D printing of the samples is reproducible for the filament spool and 3D printer used.

### 3.4. LW-PLA Findings for Different Print Size and Print Speed

The findings from the three cylindrical LW-PLA samples with diameters of 1.5 cm, 3.5 cm, and 5.5 cm are presented in Table 6. One-way ANOVA tests revealed statistically significant differences between each group for the mean HU, $STD_{xy}$, and $STD_z$. The 5.5 cm diameter sample is responsible for the observed differences in the mean HU values, while all groups contribute to the differences observed in the $STD_{xy}$ and $STD_z$ values.
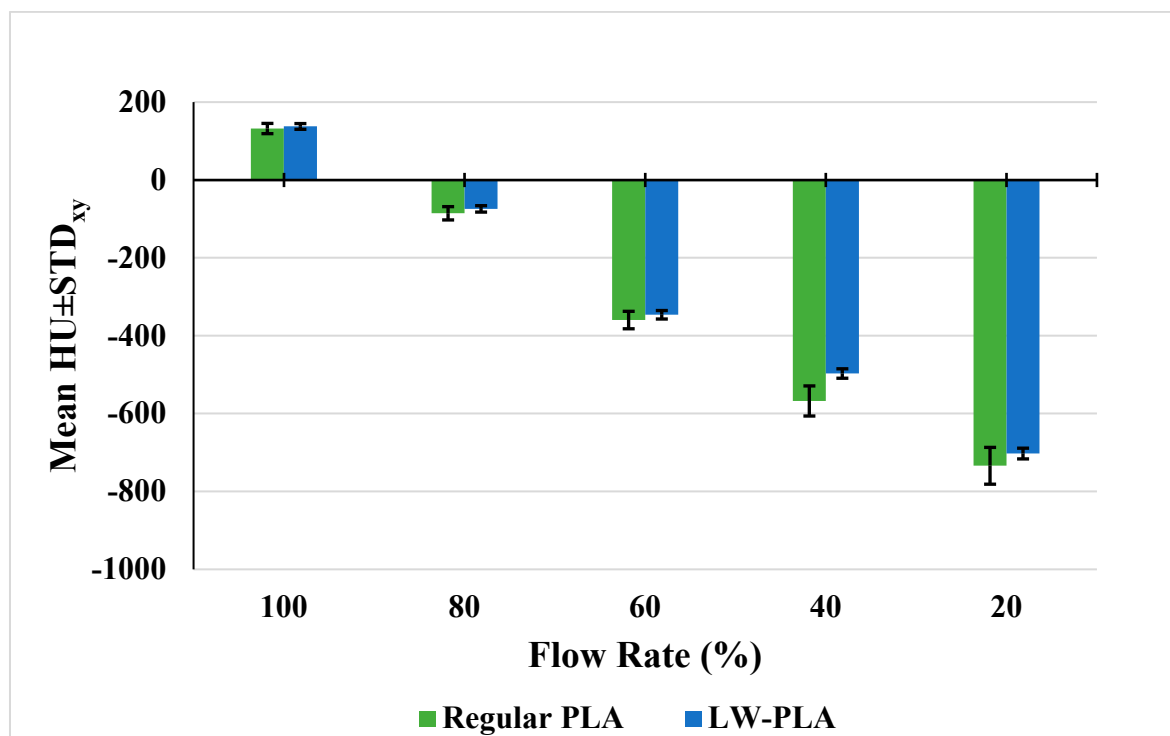
**Figure 10.** Comparison of $STD_{xy}$ values of the samples printed with regular PLA and LW-PLA having similar mean HU.

**Table 5.** Reproducibility assessment of the printing jobs. $HU_1$ refers to the mean HU value of the first printing job, $HU_2$ refers to the mean HU value of the second printing job, and $HU_3$ refers to the mean HU value of the third printing job. '$\pm STD$' denotes the standard deviation calculated across these three HU values.

| Printing Temperature (°C) | Flow Rate (%) | $HU_1$ | $HU_2$ | $HU_3$ | $\frac{HU_1+HU_2+HU_3}{3}$ | $\pm STD$ |
|---|---|---|---|---|---|---|
| | 100 | 138.9 | 137.6 | 136.7 | 137.7 | 1.1 |
| | 90 | 7.7 | 4.0 | 5.7 | 5.8 | 1.8 |
| 210 | 80 | −113.5 | −116.3 | −116.3 | −115.4 | 1.6 |
| | 70 | −228.6 | −237.1 | −235.4 | −233.7 | 4.5 |
| | 60 | −347.8 | −346.1 | −353.8 | −349.2 | 4.0 |
| | 80 | −98.7 | −103.3 | −99.8 | −100.6 | 2.4 |
| | 70 | −195.3 | −205.2 | −197.5 | −199.3 | 5.2 |
| 230 | 60 | −284.2 | −295.8 | −291.8 | −290.6 | 5.9 |
| | 50 | −390.9 | −390.1 | −387.9 | −389.6 | 1.6 |
| | 40 | −497.1 | −486.3 | −494.6 | −492.7 | 5.6 |
| | 60 | −304.7 | −301.2 | −295.7 | −300.5 | 4.5 |
| | 50 | −386.0 | −391.8 | −384.0 | −387.3 | 4.1 |
| 250 | 40 | −475.8 | −478.4 | −473.3 | −475.8 | 2.6 |
| | 30 | −599.3 | −602.2 | −598.7 | −600.1 | 1.8 |
| | 20 | −702.7 | −708.0 | −704.0 | −704.9 | 2.7 |

**Table 6.** Mass, density, mean HU, STD$_{xy}$, and STD$_z$ findings of cylindrical LW-PLA samples printed at 27 mm/s print speed with different diameters.

| Diameter (cm) | Mass (g) | Density (g/cm$^3$) | Mean HU | STD$_{xy}$ | STD$_z$ |
|---|---|---|---|---|---|
| 1.5 | 1.53 | 0.43 | −589.1 | 9.2 | 2.5 |
| 3.5 | 8.33 | 0.43 | −587.4 | 7.3 | 3.7 |
| 5.5 | 20.6 | 0.43 | −581.4 | 6.1 | 2.7 |

These three samples were printed using a printing temperature of 250 °C, a flow rate of 60%, and a print speed of 27 mm/s, which differs from the other samples printed at 33 mm/s. When compared with the 1.5 cm diameter sample printed at 250 °C, a 60% flow rate, and 33 mm/s (Table 2), the sample printed at 27 mm/s resulted in a significantly lower density and mean HU value, almost halved.

## 4. Discussion

The manufacture of 3D-printed imaging and dosimetry phantoms, as alternatives to commercial phantoms, is an emerging field of research in medical physics. Despite concerns about the calibration and standardization of in-house 3D printing processes, advances in printing techniques and materials support the belief that 3D-printed phantoms may replace commercial phantoms in clinical quality assurance procedures [28]. One of these printing techniques, FDM technology, offers users remarkable opportunities to mimic the radiological properties of most of the biological tissues via 3D printing. Numerous studies have investigated the impact of different printing materials and parameters on the radiological characterization of 3D-printed objects. These endeavors have introduced a wide range of materials and methods, with the goal of reproducing the radiological properties of various tissues. However, a common limitation is reported in the majority of these studies, which is associated with the use of low infill percentages in mimicking low-density tissues such as the lungs [18,21–24,29].

In this study, we investigated and introduced a novel technique for density modulation using a special filament, LW-PLA. Distinguished from regular PLA filaments, LW-PLA exhibits a foaming feature at printing temperatures above 220 °C. This unique characteristic offers users the opportunity to adjust the density of a printing job at the nozzle exit rather than on the print bed. Consequently, it allows for the production of print jobs with a significantly lower density, even when printed at 100% infill. To the best of our knowledge, there are no published studies on the radiological characterization of this type of filament or its associated printing technique.

The framework of this study was established based on the utilization of high printing temperatures to facilitate the expansion of LW-PLA. This phenomenon is expected to become dominant at high temperatures starting from around 220 °C. Therefore, the choice of high flow rates together with high temperatures may increase the magnitude of expansion experienced by the filament to such a point that it can deteriorate the geometric accuracy of the print job. An illustrative example of this issue is presented in Figure 2, showcasing a sample printed at 250 °C with a 100% flow rate. Therefore, to prevent overexpansion and maintain the geometric accuracy of the printed samples, the maximum applied flow rate was reduced by 10% each time the printing temperature was increased by 10 °C.

The findings of the LW-PLA samples are illustrated in Table 2. The density of the cylindrical samples varied between 0.36 g/cm$^3$ and 1.21 g/cm$^3$. The lowest density was observed for the sample printed at 250 °C with a 20% flow rate, while the highest density was observed for the sample printed at 210 °C with a 100% flow rate. These results demonstrate a reduction in the density of up to 70% for the same printing material with a constant infill of 100%. As expected, strong linear correlations were observed between the flow rate and density at all printing temperatures ($R^2 > 0.99$). Additionally, the findings from the regular PLA samples, printed at 230 °C with different flow rates between 100% and 20%, showed very similar densities, as given in Table 3.

CT scans of the LW-PLA samples revealed mean Hounsfield Unit (HU) values ranging from $-702.7$ HU to $+141.4$ HU. Similarly, the regular PLA samples yielded comparable results. However, the $STD_{xy}$ values obtained from the regular PLA samples were expectedly found to be higher than the values observed in the LW-PLA samples. The magnitude of this difference reaches threefold for the flow rate of 20%, as indicated in Table 4. These results demonstrate that, due to its foaming feature, the LW-PLA filament is superior to regular PLA filaments in printing low-density parts with a homogeneous texture.

The axial and longitudinal homogeneity ($STD_{xy}$ and $STD_z$) of the LW-PLA samples were statistically evaluated, and neither of the STD datasets showed any correlation with the flow rate, printing temperature, or mean HU. For $STD_{xy}$, the median value was $\pm 9.3$ HU, with a third quartile value of $\pm 11.9$ HU. This suggests that, for the majority of the printing jobs, the axial homogeneity is comparable to that of distilled water, measured at $\pm 7.5$ HU. On the other hand, the $STD_z$ of the LW-PLA samples ranged from $\pm 1.1$ HU to $\pm 9.0$ HU, with a median of $\pm 5.4$ HU, while that of the regular PLA samples was observed up to $\pm 10$ HU, with a median of $\pm 8.4$ HU. For water, the $STD_z$ was recorded as $\pm 0.6$ HU. These findings imply that the homogeneity of 3D-printed samples along the longitudinal axis is slightly below the reference level measured in water, regardless of the filament used. This could potentially be attributed to the minor fluctuations that may occur in the printing parameters during the printing process.

The LW-PLA filament is sensitive to changes in the exerted heat energy, primarily governed by the printing temperature, flow rate, and print speed. Additionally, the axial dimensions of the print job can be considered as an important factor influencing the heat transfer experienced by consecutive layers. For this reason, the cylindrical LW-PLA samples were printed with different diameters and at a lower speed than the previous print jobs (27 mm/s print speed used instead of 33 mm/s) to investigate the effects of the sample dimensions and print speed on the radiological property.

The results revealed that the print speed plays an important role in the physical and radiological properties of a print job. It was observed that reducing the print speed from 33 mm/s to 27 mm/s for the sample printed at 250 °C and a 60% flow rate resulted in an almost 50% reduction in both the physical density and mean HU value. This difference can be explained by defining the relationship between the print speed and absolute volumetric flow rate, rather than the percent flow rate, which is defined as a multiplier of the absolute volumetric flow rate.

For a print job, the absolute volumetric flow rate is determined by the multiplication of three factors, which are the layer height, line width, and print speed. So, reducing the print speed while keeping the layer height and line width constant would result in a reduction in the absolute volumetric flow rate as well. This is clearly indicated by the mass measurements taken from the samples. The sample printed at 250 °C, a 60% flow rate, and 33 mm/s weighed 2.72 g, while the sample printed at an identical printing temperature and percent flow rate but at a 27 mm/s print speed weighed 1.53 g. This shows that, despite keeping the percent flow rate constant at 60%, the absolute volumetric flow rate decreased due to the execution of a lower print speed, resulting in the extrusion of less amount of filament.

The statistical analyses conducted across the findings of the print jobs with different diameters revealed significant reductions in the $STD_x$ values with the increasing diameter of the print job. Additionally, the mean HU value of the sample with a 5.5 cm diameter ($-582.4$ HU) was found to be significantly lower than the mean HU values of the other two samples ($-589.1$ HU and $-587.4$ HU). Although statistically significant, this difference corresponds to a relative difference of 1.1% and does not represent a critical change. The $STD_z$, on the other hand, was observed to change arbitrarily among the samples, suggesting that it does not depend on the dimensions of the print job.

The reproducibility of the print job was analyzed, and similar HU values were consistently obtained for the repeated printing jobs at 210 °C, 230 °C, and 250 °C, as illustrated in Table 5. The most significant absolute difference occurred between the first and second

printing jobs performed at 230 °C with a 60% flow rate, corresponding to a relative difference of 4%. The majority of samples exhibited HU values remaining within one standard deviation of the average HU, recorded as $\pm 5.9$ at most. These findings indicate that the printing jobs are reproducible, as supported by strong correlations ($R^2 > 0.99$) between the flow rate and mean HU at all printing temperatures, as depicted in Figure 6.

The HU range achieved in this study suggests that the LW-PLA filament is capable of replicating the radiological properties of most tissues and organs, as illustrated in Figure 7. This excludes only compact bones and low-density portions of the lungs, which have HU values beyond +350 HU and around −900 HU, respectively [30,31]. Nevertheless, our findings suggest that low-density lung-equivalent samples could be successfully achieved via the further adjustment of the printing parameters, especially the print speed. The selection of a layer thickness higher than 0.15 mm can also contribute to a further reduction in the density, as reported in the literature [12]. Finally, a slight reduction in the infill percentage could be considered to achieve lower HU values while ensuring that the homogeneity (i.e., STD) of the sample remains at an acceptable level.

Importantly, this study demonstrated a significantly improved homogeneity in the lower Hounsfield Unit (HU) range compared to studies where a similar HU range is achieved by controlling the infill percentage. For instance, Madamesila et al. used a high-impact polystyrene (HIPS) filament in their study to 3D print low- and high-density lung inserts with reduced infill percentages. Following CT imaging with a resolution of 0.5 mm × 0.5 mm × 0.4 mm, they reported mean HU values comparable to those of a commercial phantom, recorded as −826 HU and −483 HU. However, the $STD_{xy}$ value was found to be $\pm 120$ HU for the 3D-printed lung low insert, which is far beyond the $\pm 17$ HU observed in the commercial phantom [19]. Other studies also reported similar limitations due to a reduced infill percentage [18,21–24,29]. Dancewicz et al., on the other hand, conducted a similar study with a variety of filaments, including regular PLA, photoluminescent PLA, and ABS, for printing soft-tissue-equivalent inserts as an alternative to a commercial Gammex phantom. Differently from former studies, they conducted a CT scan with a relatively lower spatial resolution of 1.37 mm × 1.37 mm × 2 mm and reported $STD_{xy}$ values between $\pm 1$ HU and $\pm 14$ HU for 3D-printed inserts with mean HU values between −580 HU and −900 HU [14]. Tino et al. designed and printed gyroid structures with different geometric parameters and obtained −874 HU samples with an $STD_{xy}$ of $\pm 23$ HU following a CT scan at 140 kVp with a spatial resolution of 1.17 mm × 1.17 mm × 3 mm [32]. These results highlight the impact of different CT imaging protocols, especially on the $STD_{xy}$ values of the scanned objects. It is known that image noise can be significantly reduced by selecting lower spatial resolution settings. Leary et al. reported up to a 20-fold difference in the $STD_{xy}$ for identical samples scanned at different spatial resolution settings of 0.24 mm × 0.24 mm × 1 mm and 1.17 mm × 1.17 mm × 3 [33]. In our study, we implemented a CT protocol established for cardiovascular head and neck exams, performed at a relatively higher spatial resolution when compared to other clinical CT imaging tasks. Accordingly, CT images of the samples were acquired at 120 kVp and 310 mAs, with a spatial resolution of 0.488 mm × 0.488 mm × 0.4 mm.

There are a number of studies that achieved a low HU range with better homogeneities by either using different filaments or adjusting parameters other than the infill percentage [15,25,26]. Kozee et al. used an ultralight polypropylene (PP) filament with a density of 0.75 g/cm$^3$ and printed lung models with 25% infill, corresponding to −829.6 ± 33.7 HU [15]. However, one drawback about a PP filament is that it is not suitable for use to print soft tissues due to its low density. LW-PLA, on the other hand, can be used for both the lungs and other soft tissues. Okkalidis et al. developed a software that modulates the flow rate during a printing job [25]. Mei et al. developed a similar software that, instead of the flow rate, modulates the printing speed during a printing job [26]. Both studies achieved realistic lung textures by meticulously controlling the width of the printed lines at subpixel dimensions. However, these algorithms are not readily available, and developing similar algorithms could pose a challenging task for most researchers. In

addition, the use of LW-PLA could both shorten the printing time and reduce the amount of filament material required for a similar printing job.

## 5. Conclusions

In this study, we introduced a novel density modulation technique with a new kind of filament. It is shown that a wide range of HU could be achieved, covering almost all of the soft tissues with a significantly improved homogeneity to replicate low-density textures. This innovative approach offers practical and accessible means to fabricate low-density tissue-mimicking phantoms for medical applications, addressing a critical need in the field of 3D printing for medical physics.

## References

1. Haleem, A.; Javaid, M.; Suman, R.; Singh, R.P. 3D Printing Applications for Radiology: An Overview. *Indian J. Radiol. Imaging* **2021**, *31*, 10–17. Available online: http://www.ncbi.nlm.nih.gov/pubmed/34316106 (accessed on 20 November 2023). [PubMed]
2. Tino, R.; Yeo, A.; Leary, M.; Brandt, M.; Kron, T. A systematic review on 3D-Printed imaging and dosimetry phantoms in radiation therapy. *Technol. Cancer Res. Treat.* **2019**, *18*, 1–14. [CrossRef] [PubMed]
3. Filippou, V.; Tsoumpas, C. Recent advances on the development of phantoms using 3D printing for imaging with CT, MRI, PET, SPECT, and ultrasound. *Med. Phys.* **2018**, *45*, e740–e760. [CrossRef] [PubMed]
4. McGarry, C.K.; Grattan, L.J.; Ivory, A.M.; Leek, F.; Liney, G.P.; Liu, Y.; Miloro, P.; Rai, R.; Robinson, A.P.; Shih, A.J.; et al. Tissue mimicking materials for imaging and therapy phantoms: A review. *Phys. Med. Biol.* **2020**, *65*, 23TR01. [CrossRef] [PubMed]
5. Bibb, R.; Thompson, D.; Winder, J. Computed tomography characterisation of additive manufacturing materials. *Med. Eng. Phys.* **2011**, *33*, 590–596. [CrossRef]
6. Shin, J.; Sandhu, R.S.; Shih, G. Imaging Properties of 3D Printed Materials: Multi-Energy CT of Filament Polymers. *J. Digit. Imaging* **2017**, *30*, 572–575. [CrossRef]
7. Alssabbagh, M.; Tajuddin, A.A.; Manap, M.b.A.; Zainon, R. Evaluation of nine 3D printing materials as tissue equivalent materials in terms of mass attenuation coefficient and mass density. *Int. J. Adv. Appl. Sci.* **2017**, *4*, 168–173. Available online: http://www.science-gate.com/IJAAS/V4I9/Alssabbagh.html (accessed on 20 November 2023). [CrossRef]
8. Solc, J.; Vrba, T.; Burianova, L. Tissue-equivalence of 3D-printed plastics for medical phantoms in radiology. *J. Instrum.* **2018**, *13*, P09018. [CrossRef]
9. Ivanov, D.; Bliznakova, K.; Buliev, I.; Popov, P.; Mettivier, G.; Russo, P.; Di Lillo, F.; Sarno, A.; Vignero, J.; Bosmans, H.; et al. Suitability of low density materials for 3D printing of physical breast phantoms. *Phys. Med. Biol.* **2018**, *63*, 175020. [CrossRef]
10. Assemany, L.P.F.; Rodrigues, O.; da Silva, E.; Potiens, M.d.P.A. Evaluation of 3D printing filaments for construction of a pediatric phantom for dosimetry in CBCT. *Radiat. Phys. Chem.* **2020**, *167*, 108227. [CrossRef]
11. Kalender, W.A. *Computed Tomography: Fundamentals, System Technology, Image Quality, Applications*, 3rd ed.; Publicis: Paris, France, 2011.
12. Ma, X.; Buschmann, M.; Unger, E.; Homolka, P. Classification of X-ray Attenuation Properties of Additive Manufacturing and 3D Printing Materials Using Computed Tomography from 70 to 140 kVp. *Front. Bioeng. Biotechnol.* **2021**, *9*, 763960. [CrossRef] [PubMed]
13. Yeo, A.; Brandt, M.; Leary, M.; Kron, T.; Tino, R. The interlace deposition method of bone equivalent material extrusion 3D printing for imaging in radiotherapy. *Mater. Des.* **2021**, *199*, 109439. [CrossRef]
14. Dancewicz, O.L.; Sylvander, S.R.; Markwell, T.S.; Crowe, S.B.; Trapp, J.V. Radiological properties of 3D printed materials in kilovoltage and megavoltage photon beams. *Phys. Med.* **2017**, *38*, 111–118. [CrossRef] [PubMed]

15. Kozee, M.; Weygand, J.; Andreozzi, J.M.; Hunt, D.; Perez, B.A.; Graham, J.A.; Redler, G. Methodology for computed tomography characterization of commercially available 3D printing materials for use in radiology/radiation oncology. *J. Appl. Clin. Med. Phys.* **2023**, *24*, e13999. [CrossRef] [PubMed]

16. Ceh, J.; Youd, T.; Mastrovich, Z.; Peterson, C.; Khan, S.; Sasser, T.A.; Sander, I.M.; Doney, J.; Turner, C.; Leevy, W.M. Bismuth infusion of ABS enables additive manufacturing of complex radiological phantoms and shielding equipmen. *Sensors* **2017**, *17*, 459. [CrossRef] [PubMed]

17. Hamedani, B.A.; Melvin, A.; Vaheesan, K.; Gadani, S.; Pereira, K.; Hall, A.F. Three-dimensional printing CT-derived objects with controllable radiopacity. *J. Appl. Clin. Med. Phys.* **2018**, *19*, 317–328. [CrossRef] [PubMed]

18. Kairn, T.; Crowe, S.B.; Markwell, T. Use of 3D printed materials as tissue-equivalent phantoms. In *IFMBE Proceedings*; Springer: New York, NY, USA, 2015; pp. 728–731.

19. Madamesila, J.; McGeachy, P.; Villarreal Barajas, J.E.; Khan, R. Characterizing 3D printing in the fabrication of variable density phantoms for quality assurance of radiotherapy. *Phys. Med.* **2016**, *32*, 242–247. [CrossRef]

20. Negus, I.S.; Holmes, R.B.; Jordan, K.C.; Nash, D.A.; Thorne, G.C.; Saunders, M. Technical Note: Development of a 3D printed subresolution sandwich phantom for validation of brain SPECT analysis. *Med. Phys.* **2016**, *43*, 5020–5027. [CrossRef]

21. Mille, M.M.; Griffin, K.T.; Maass-Moreno, R.; Lee, C. Fabrication of a pediatric torso phantom with multiple tissues represented using a dual nozzle thermoplastic 3D printe. *J. Appl. Clin. Med. Phys.* **2020**, *21*, 226–236. [CrossRef]

22. Hong, D.; Lee, S.; Kim, G.B.; Lee, S.M.; Kim, N.; Seo, J.B. Development of a CT imaging phantom of anthromorphic lung using fused deposition modeling 3D printing. *Medicine* **2020**, *99*, e18617. [CrossRef]

23. Okkalidis, N.; Chatzigeorgiou, C.; Okkalides, D. Assessment of 11 Available Materials With Custom Three-Dimensional-Printing Patterns for the Simulation of Muscle, Fat, and Lung Hounsfield Units in Patient-Specific Phantoms. *J. Eng. Sci. Med. Diagn. Ther.* **2018**, *1*, 011003. [CrossRef]

24. Cavaliere, C.; Baldi, D.; Brancato, V.; Aiello, M.; Salvatore, M. A customized anthropomorphic 3D-printed phantom to re-producibility assessment in computed tomography: An oncological case study. *Front. Oncol.* **2023**, *13*, 1123796. [CrossRef] [PubMed]

25. Okkalidis, N. A novel 3D printing method for accurate anatomy replication in patient specific phantoms. *Med. Phys.* **2018**, *45*, 4600–4606. [CrossRef] [PubMed]

26. Mei, K.; Geagan, M.; Roshkovan, L.; Litt, H.I.; Gang, G.J.; Shapira, N.; Stayman, J.W.; Noël, P.B. Three-dimensional printing of patient-specific lung phantoms for CT imaging: Emulating lung tissue with accurate attenuation profiles and textures. *Med. Phys.* **2022**, *49*, 825–835. [CrossRef] [PubMed]

27. Available online: https://deckard.duhs.duke.edu/~samei/tg233.html (accessed on 18 November 2023).

28. Ehler, E.; Craft, D.; Rong, Y. 3D printing technology will eventually eliminate the need of purchasing commercial phantoms for clinical medical physics QA procedures. *J. Appl. Clin. Med. Phys.* **2018**, *19*, 8–12. [CrossRef] [PubMed]

29. Craft, D.F.; Howell, R.M. Preparation and fabrication of a full-scale, sagittal-sliced, 3D-printed, patient-specific radiotherapy phantom. *J. Appl. Clin. Med. Phys.* **2017**, *18*, 285–292. [CrossRef]

30. Ma, X.; Figl, M.; Unger, E.; Buschmann, M.; Homolka, P. OPEN X-ray attenuation of bone, soft and adipose tissue in CT from 70 to 140 kV and comparison with 3D printable additive manufacturing materials. *Sci. Rep.* **2022**, *12*, 14580. [CrossRef]

31. Mazzilli, A.; Fiorino, C.; Loria, A.; Mori, M.; Esposito, P.G.; Palumbo, D.; de Cobelli, F.; del Vecchio, A. An Automatic Approach for Individual HU-Based Characterization of Lungs in COVID-19 Patients. *Appl. Sci.* **2021**, *11*, 1238. [CrossRef]

32. Tino, R.; Leary, M.; Yeo, A.; Brandt, M.; Kron, T. Gyroid structures for 3D-printed heterogeneous radiotherapy phantoms. *Phys. Med. Biol.* **2019**, *64*, 21NT05. [CrossRef]

33. Leary, M.; Keller, C.; Yeo, A. Additive Manufacture of Lung Equivalent Anthropomorphic Phantoms: A Method to Control Hounsfield Number Utilizing Partial Volume Effect. *J. Eng. Sci. Med. Diagn. Ther.* **2020**, *3*, 011001. [CrossRef]